



Whole-brain propagating patterns in human resting-state brain activities

Yusuke Takeda^{a,b,*}, Nobuo Hiroe^b, Okito Yamashita^{a,b}

^a Computational Brain Dynamics Team, RIKEN Center for Advanced Intelligence Project, 2-2-2 Hikaridai, Seika-cho, Soraku-gun, Kyoto 619-0288, Japan

^b Department of Computational Brain Imaging, ATR Neural Information Analysis Laboratories, 2-2-2 Hikaridai, Seika-cho, Soraku-gun, Kyoto 619-0288, Japan



ARTICLE INFO

Keywords:

Resting-state
Whole-brain propagating activity
Spatiotemporal pattern
Resting-state network
Magnetoencephalography (MEG)
Electroencephalography (EEG)

ABSTRACT

Repetitive propagating activities in resting-state brain activities have been widely observed in various species and regions. Because they resemble the preceding brain activities during tasks, they are assumed to reflect past experiences embedded in neuronal circuits. “Whole-brain” propagating activities may also reflect a process that integrates information distributed over the entire brain, such as visual and motor information. Here we reveal whole-brain propagating activities from human resting-state magnetoencephalography (MEG) and electroencephalography (EEG) data. We simultaneously recorded the MEGs and EEGs and estimated the source currents from both measurements. Then using our recently proposed algorithm, we extracted repetitive spatiotemporal patterns from the source currents. The estimated patterns consisted of multiple frequency components, each of which transiently exhibited the frequency-specific resting-state networks (RSNs) of functional MRIs (fMRIs), such as the default mode and sensorimotor networks. A simulation test suggested that the spatiotemporal patterns reflected the phase alignment of the multiple frequency oscillators induced by the propagating activities along the anatomical connectivity. These results argue that whole-brain propagating activities transiently exhibited multiple RSNs in their multiple frequency components, suggesting that they reflected a process to integrate the information distributed over the frequencies and networks.

1. Introduction

Over the last two decades, resting-state (or spontaneous) brain activities have attracted much interest in the neuroscience community. They are shown to be not random; they are structured in space and time (e.g., Zalesky et al., 2014).

In nonhuman studies, repetitive spatiotemporal patterns in resting-state brain activities have been widely observed in various species and regions, such as rat and mouse hippocampal place cells (Dragoi and Tonegawa, 2011; Ji and Wilson, 2007; Wilson and McNaughton, 1994) and rat and cat visual cortices (Han et al., 2008; Ikegaya et al., 2004; Ji and Wilson, 2007). Theoretical studies have argued that such patterns are formed by propagating activities along strong anatomical connections (Izhikevich et al., 2004; Teramae et al., 2012). Because the patterns resemble the preceding brain activities during tasks, they probably reflect past experiences embedded in neuronal circuits (Han et al., 2008; Ji and Wilson, 2007; Wilson and McNaughton, 1994). On the other hand, “whole-brain” propagating activities were also observed in mice (Matsui et al., 2016), perhaps reflecting a process that integrates the information distributed over the entire brain, such as visual and motor information.

In this paper, we define propagating activity and spatiotemporal patterns as follows. Propagating activity is literally the brain activity that circulates through anatomical connections. Spatiotemporal patterns are observations represented by the two-dimensional matrices of space \times time (Supplementary material, SFig. 1). Propagating activities generate spatiotemporal patterns in brain measurement data, such as calcium imaging. Therefore, propagating activity and spatiotemporal patterns share a cause and effect relationship.

Human studies have also examined propagating activities from resting-state functional MRIs (fMRIs). Using a template matching algorithm, Majeed et al. (2011) identified repetitive spatiotemporal patterns that consist of an alteration between the activation of the default mode network (DMN) and the task-positive network. We also extracted repetitive spatiotemporal patterns from over 1,000 subjects’ resting-state fMRIs including subjects with autism spectrum disorder (ASD) and typically developed individuals and examined the differences in the patterns between the groups (Takeda et al., 2019a). Using temporal lag analyses, Mitra et al. (2014), Mitra et al. (2015a,b), Mitra and Raichle (2016) extensively examined the temporal structures of propagating fMRI signals. However, because fMRIs measure hemodynamic responses to neuronal activities and the responses are slow, it is difficult to identify neuronal propagating activities in the millisecond order from fMRIs.

* Corresponding author at: Computational Brain Dynamics Team, RIKEN Center for Advanced Intelligence Project, 2-2-2 Hikaridai, Seika-cho, Soraku-gun, Kyoto 619-0288, Japan.

<https://doi.org/10.1016/j.neuroimage.2021.118711>.

Received 9 August 2021; Received in revised form 15 October 2021; Accepted 4 November 2021

Available online 16 November 2021.

1053-8119/© 2021 The Author(s). Published by Elsevier Inc. This is an open access article under the CC BY-NC-ND license

(<http://creativecommons.org/licenses/by-nc-nd/4.0/>)

On the other hand, human electrophysiological studies have examined propagating activities with fine temporal resolution. Electroencephalography (EEG) studies suggested the existence of whole-brain propagating activities based on sensor space analyses (Ito et al., 2005; 2007; Massimini et al., 2004). Electrocochography (ECoG) studies revealed propagating activities at the motor and temporal cortices (Muller et al., 2018; 2016; Takahashi et al., 2011). A magnetoencephalography (MEG) study revealed the temporal structure of alpha band (8–13 Hz) activities using temporal lag analysis (Basti et al., 2019). However, spatiotemporal patterns formed by whole-brain propagating activities remain hidden in human resting-state electrophysiological studies.

Conventionally, MEG/EEG studies have examined spatiotemporal patterns that are time-locked to external stimulus onsets: event-related fields/potentials. Such patterns provide rich information about the propagating activities driven by the stimuli, such as the time and place information of signal flows. In the case of resting-states, however, such patterns are difficult to extract because resting-state data do not have overt stimulus or response onsets; the patterns' onsets are also unknown. To solve this problem, we developed a method called SpatioTemporal Pattern estimation (STeP) (Takeda et al., 2016). From resting-state brain activity data, STeP simultaneously estimates repetitive spatiotemporal patterns and their onsets by alternately iterating the updates of the shapes and onsets of the patterns. More recently, we extended STeP for big data (BigSTeP) (Takeda et al., 2019a). From many or long resting-state data, BigSTeP estimates spatiotemporal patterns with less computation cost than STeP.

In this study, we reveal spatiotemporal patterns generated by whole-brain propagating activities from human resting-state MEG and EEG data. We simultaneously recorded the MEGs and EEGs and estimated the source currents from both measurements. Then using BigSTeP, we extracted repetitive spatiotemporal patterns from the source currents and examined their temporal frequencies and spatial similarities with fMRI's resting-state networks (RSNs). Finally, we conducted a simulation test to examine how the spatiotemporal patterns were generated from propagating activities along the anatomical connectivity. These analyses revealed the whole-brain propagating activities, which transiently exhibited multiple RSNs in their multiple frequency components, suggesting that they reflected a process to integrate the information distributed over the frequencies and the networks.

2. Materials and methods

2.1. MEG-EEG experiment

Twelve healthy subjects [2 females, 26.8 ± 7.8 (mean \pm standard deviation [SD]) years old] participated in our MEG-EEG experiment. All subjects gave written informed consent for the experimental procedures, which were approved by the ATR Human Subject Review Committee.

They performed a resting-state task for two runs. In this task, they fixated on a cross for 5 min.

During the task, we simultaneously recorded their MEGs and EEGs with a whole-head, 400-channel system (210-channel Axial and 190-channel Planar Gradiometers; PQ1400RM; Yokogawa Electric Co., Japan) and a whole-head, 63-channel system (BrainAmp; Brain Products GmbH, Germany), respectively. The EEG electrodes were placed according to the extended 10–20 system using FPz and FCz as a ground and a reference, respectively. Electrooculograms (EOGs) were also recorded simultaneously. The sampling frequency was 1 kHz.

2.2. MRI experiment

The subjects also participated in an MRI experiment to record their T1-weighted images. They again gave written informed consent for the experimental procedures, which were approved by the ATR Human Subject Review Committee.

The T1-weighted images were recorded by three Tesla MR scanner (MAGNETOM Trio 3T; Siemens, Germany) with the following acquisition parameters: 2250-ms repetition time; 3.06 ms echo time; 9-degree flip angle; 1 mm thick slices; 256×256 mm field of view; and 256×256 imaging matrix with 208 slices.

2.3. Preprocessing MEG and EEG data

To preprocess the MEG and EEG data, we used Variational Bayesian Multimodal EncephaloGraphy (VBMEG) v2.2 (Sato et al., 2004; Takeda et al., 2019b; Yoshioka et al., 2008), which is a MATLAB toolbox for MEG/EEG source imaging (<https://vbmeg.atr.jp/>). Using reference sensor data in the MEG, environmental noise was removed from the MEG data by time-shift principal component analysis (PCA) (de Cheveigné and Simon, 2007). The MEG and EEG data were passed through a low-pass finite impulse response (FIR) filter with a cutoff frequency of 50 Hz, sampled at 500 Hz, and passed through a high-pass FIR filter with a 0.4-Hz cutoff frequency. The EOG artifacts were regressed out for each sensor. Cardiac artifacts and sensor noise were removed by independent component analysis (ICA) (Jung et al., 2001). We excluded the sensors whose powers exceeded their mean + $10 \times$ SD across the sensors. For the EEG data, we applied the common average reference and made the averages of the EEG data across the sensors to 0.

2.4. Estimating source currents

From the preprocessed MEG and EEG data, we estimated the source currents at 10,004 vertices on the cortex.

First, we made leadfield matrices for the MEG and EEG data using VBMEG. We respectively constructed 1-shell (cerebrospinal fluid [CSF]) and 3-shell (CSF, skull, and scalp) head conductivity models for the MEG and EEG data. Based on the models, we made leadfield matrices by solving the Maxwell equations with a boundary element method (BEM). Here we assumed three-dimensional current dipoles parallel to the x , y , and z axes.

Then, we estimated the source currents by a linearly constrained minimum variance (LCMV) beamformer (Van Veen et al., 1997). For each axis, the current was estimated by

$$q(v, t) = \mathbf{w}_v \mathbf{m}(t),$$

where $q(v, t)$ is the current at vertex v and time t , \mathbf{w}_v is the $1 \times (N_m + N_e)$ inverse filter, N_m is the number of MEG sensors, N_e is the number of EEG sensors, and $\mathbf{m}(t)$ is a $(N_m + N_e) \times 1$ data vector containing the MEG and EEG data at time t . To accommodate the different scales between the MEG and EEG data, the data and their leadfields were normalized by the leadfield norms (Henson et al., 2011; Takeda et al., 2019b). The inverse filter was obtained by

$$\mathbf{w}_v = [\mathbf{h}_v^T \tilde{\mathbf{C}}^{-1} \mathbf{h}_v]^{-1} \mathbf{h}_v^T \tilde{\mathbf{C}}^{-1},$$

where

$$\tilde{\mathbf{C}} = \mathbf{C} + \lambda \mathbf{I}.$$

\mathbf{h}_v is the $(N_m + N_e) \times 1$ leadfield vector containing the MEG and EEG's leadfields for vertex v . \mathbf{C} is the $(N_m + N_e) \times (N_m + N_e)$ covariance matrix computed between all sensor pairs. λ is a regularization constant computed by

$$\lambda = \frac{\text{tr} \mathbf{C}}{N_m + N_e} \times 0.1.$$

For each vertex, we projected the timeseries along the dipole direction to explain the most variance using singular value decomposition (SVD) (Baselice et al., 2019; Sorrentino et al., 2020). Then we normalized it to have mean 0 and SD 1 to focus on the temporal changes in each vertex induced by the whole-brain propagating activities.

2.5. Estimating repetitive spatiotemporal patterns

To reveal the whole-brain propagating activities, we extracted the repetitive spatiotemporal patterns from each subjects' source current by BigSTeP (Takeda et al., 2019a). BigSTeP was originally developed to estimate common and subject-specific spatiotemporal patterns from many subjects' resting-state data. It is also useful for long data if they are divided into short segments, which are regarded as subjects in the BigSTeP framework. In this study, we divided the source currents into 10-s segments. Each segment was assumed to contain several unknown spatiotemporal patterns at unknown onsets (Supplementary material, SFig. 1), expressed as

$$y_s(v, t) = \sum_{k=1}^K \sum_{n=1}^N p_k(v, t) u_{s,k}(t - n + 1) + z_s(v, t),$$

where $y_s(v, t)$ is the source current in segment s at vertex v and time t , K is the number of spatiotemporal patterns, N is their lengths, $p_k(v, t)$ is the k -th spatiotemporal pattern common across the segments, and $z_s(v, t)$ is noise. $u_{s,k}(t)$ is the onset timeseries of the k -th spatiotemporal pattern, expressed as

$$u_{s,k}(t) = \begin{cases} 1 & \text{onset of } k\text{-th spatiotemporal pattern} \\ 0 & \text{otherwise.} \end{cases}$$

Given number K and length N of the spatiotemporal patterns, BigSTeP estimated spatiotemporal patterns $p_k(v, t)$ and their onsets $u_{s,k}(t)$ from source current $y_s(v, t)$.

In the actual application, we reduced the computation cost by using SVD. We applied SVD to the source current, extracted the components having a cumulative contribution ratio of 0.99, and multiplied the extracted components by their singular values to keep their amplitude information. We applied BigSTeP to the dimension-reduced source current and estimated the onsets of the spatiotemporal patterns. Then from the original source current, we estimated the spatiotemporal patterns using the onsets.

The number and length of the spatiotemporal patterns were determined based on their reproducibility between the two runs. From the source current of each run, we separately estimated the spatiotemporal patterns. Then we vectorized the spatiotemporal patterns and calculated their correlation coefficient between the runs. This was repeated by changing the number from 1 to 4 and the length from 0.1 to 0.5 s. Finally, we selected the best number and length pair that achieved the highest correlation coefficient.

2.6. Examining temporal frequency of spatiotemporal patterns

To examine the temporal frequency of the estimated spatiotemporal patterns, we decomposed them into delta (0.4–4 Hz), theta (4–8 Hz), alpha (8–13 Hz), beta (13–30 Hz), and gamma (30–50 Hz) band components and calculated their powers. First, we decomposed the preprocessed MEG and EEG data into these bands using FIR filters. Second, we converted the filtered MEG and EEG data into source currents by applying the inverse filter and the normalization used in the source current estimation described above. Third, from the currents in each band, we estimated the spatiotemporal patterns using the estimated onsets. Finally, we calculated their powers by averaging the squares of the patterns across the times and vertices.

We checked the validity of this decomposing procedure by comparing the sum of the decomposed patterns with the original one. Their correlation coefficients were sufficiently high (0.998 ± 0.001), indicating that it worked well.

To check whether the powers were larger than those generated from the fluctuations that were not time-locked to the estimated onsets, we compared the powers with surrogates. The surrogate powers were generated by randomly shuffling the inter-onset intervals (IOIs) of the estimated onsets and estimating the spatiotemporal patterns using the IOI-shuffled onsets.

2.7. Evaluating spatial similarity between spatiotemporal patterns and RSNs

To evaluate the spatial similarity between the spatiotemporal patterns and the fMRI-RSNs, we calculated their correlation coefficients. We downloaded the spatial patterns of the fMRI-RSNs from BrainMap ICA (<http://brainmap.org/icns/>). For each frequency component of the patterns, we calculated the correlation coefficients between the patterns' absolute values at each time and the spatial patterns of the RSNs.

Perhaps a high correlation coefficient is attributable to the artifacts that occur when estimating the source current, such as the signal leakage (Brookes et al., 2012; Colclough et al., 2015; Sato et al., 2018). To remove this possibility, we compared the correlation coefficient with surrogates that also underwent the same artifacts. We generated 1,000 surrogate values for the correlation coefficient by estimating the patterns from the source current using the IOI-shuffled onsets. The p -value was estimated by

$$p = \frac{\#\{x_g \geq x, g = 1 : 1,000\}}{1,000}, \quad (1)$$

where x and x_g are respectively the original and g -th surrogate values.

This is the multiple comparison problem, which we solved by controlling the false discovery rate (FDR). FDR manages the expected proportion of the false positive findings among all the rejected null hypotheses (Benjamini and Hochberg, 1995). We estimated the q -values by Storey and Tibshirani's method (Storey and Tibshirani, 2003). From the distribution of the p -values, we first estimated the proportion of null p -values π_0 , and based on π_0 we converted the p -values to q -values. The FDRs were controlled at 0.01.

To summarize the results of all the subjects, we examined how frequently high correlation coefficients were observed. For each frequency band and RSN, we calculated the proportion of the significant correlation coefficients among all the times, patterns, and subjects. Since a p -value less than 0.01 was considered significant, the chance level was 0.01.

2.8. Simulating resting-state brain activities

We conducted a simulation test to examine the generating mechanism of the spatiotemporal patterns. Here we asked how the propagating activities along the human brain's anatomical connectivity form spatiotemporal patterns.

We simulated propagating brain activity using a whole-brain network model of Kuramoto oscillators (Cabral et al., 2014; Gollo et al., 2017; Pang et al., 2021). We parceled the cortex into 360 regions of interest (ROIs) according to the HCP-MMP1.0 atlas (Glasser et al., 2016). The phase dynamics of a ROI is expressed by

$$\frac{d\theta_a}{dt} = \omega_a + \kappa \sum_{b=1}^{360} E(a, b) \sin(\theta_b(t - \tau_{ab}) - \theta_a(t)), \quad (2)$$

where θ_a is the phase of ROI a , ω_a is the natural frequency of ROI a , κ is the global coupling strength, $E(a, b)$ is the connectivity strength, and τ_{ab} is the delay between ROIs a and b . In this model, we focused on the phase dynamics of limit-cycle oscillators coupled across the ROIs while ignoring their amplitudes. We determined ω_a , $E(a, b)$, and τ_{ab} based on the anatomical connectivity derived from many subjects' diffusion MRIs (dMRIs) (Rosen and Halgren, 2021). We downloaded the logarithm of connectivity f_{ab} and fiber length d_{ab} from <https://zenodo.org/record/4060485#.YKRHwS2MsWo>. Connectivity strength $E(a, b)$ was obtained by calculating the antilogarithm of f_{ab} and normalizing the resultant values so that their maximum value became 1. Based on Pang et al. (2021), natural frequency ω_a was determined by

$$\omega_a = \omega_{max} - (\omega_{max} - \omega_{min}) \left(\frac{s_a - s_{min}}{s_{max} - s_{min}} \right)^2,$$

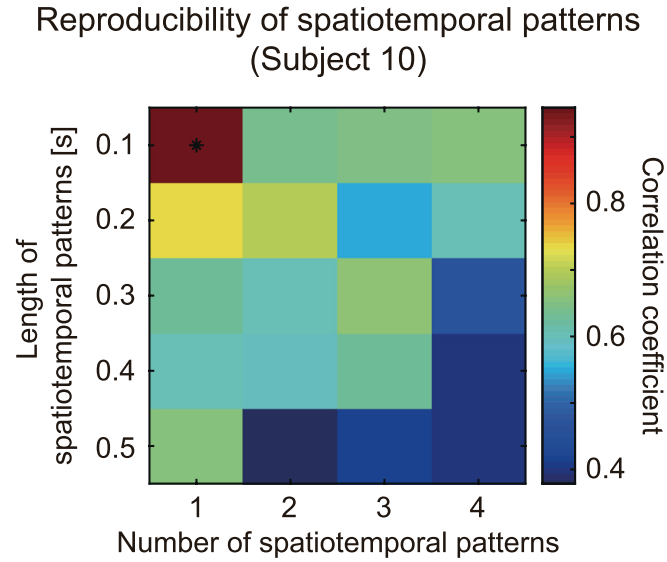


Fig. 1. Sample reproducibility of spatiotemporal patterns for each pair of hyperparameters: number and length of spatiotemporal patterns. Correlation coefficients of estimated spatiotemporal patterns between two runs are shown for subject 10. Based on this result, the number and length of spatiotemporal patterns were respectively determined to be 1 and 0.1 s for this subject.

where s_a is the ROI's connectivity strength given by $s_a = \sum_b^{360} E(a, b)$. s_{min} and s_{max} are respectively the minimum and maximum values of s_a across the ROIs. The frequency limits, ω_{min} and ω_{max} , were set to 8 and 40 Hz because transcranial magnetic stimulation (TMS) studies have suggested that natural frequencies can be found at the alpha, beta, and gamma bands in the human brain (Okazaki et al., 2021; Rosanova et al., 2009). Delay τ_{ab} was calculated by $\tau_{ab} = d_{ab}/v$, where v is the conduction velocity. We set κ to 0, 20, ..., 180, or 200 and v to 2, 4, ..., 18, or 20 m/s.

For each κ and v pair, we simulated the brain activity for 50 s using an Euler scheme with 0.1 ms time steps from the random initial values and discarded the first 20 s. The simulation was iterated 10 times with different initial values. Thus, we obtained 30 (= 50 - 20) s \times 10 simulated brain activities for each κ and v pair.

To characterize the behavior of the simulated brain activities, we calculated the synchrony degrees (Cabral et al., 2014):

$$s(t) = \left| \frac{1}{360} \sum_{a=1}^{360} \exp(i\theta_a(t)) \right|. \quad (3)$$

This value becomes 1 if the phases are identical across the ROIs and close to 0 if uniformly distributed. From the 30-s simulated brain activities, we calculated the SD of $s(t)$ across the times to capture how largely the synchrony degree fluctuated in time and quantified the system's metastability level (Cabral et al., 2014).

We also examined the width of the frequency band in the simulated brain activity. For each ROI, we detected the peak frequency from the power spectrum of $\sin(\theta_a)$. Then from the distribution of the peak frequencies, we calculated its entropy, which becomes large when the simulated brain activity was broadband.

2.9. Estimating repetitive spatiotemporal patterns from simulated brain activities

For each κ and v pair, we estimated the repetitive spatiotemporal patterns from the simulated brain activities using BigSTeP. The number and length of the patterns were set to 1 and 0.1 s based on the parameters selected for subject 10 (Fig. 1).

We evaluated the similarity of the estimated patterns with those estimated from the real data. For this purpose, we characterized the patterns

by their amplitudes because the patterns estimated from the real data had a tendency common across the subjects in their amplitudes but not in their peak times (Supplementary material, SFig. 2). For the simulated data, we averaged the patterns' absolute values across the times. For the real data, we averaged their absolute values across the times and vertices within each ROI. Then we calculated their correlation coefficients between the simulated and real data.

Perhaps a high correlation coefficient is attributable to the artifacts that occur when estimating the source current. To remove this possibility, we compared the correlation coefficient with surrogates that also underwent the same artifacts. We generated 1,000 surrogate values for the correlation coefficients by shuffling the ROIs in the simulated brain activity while keeping the correspondence between the left and right hemispheres. The p -value was estimated by Eq. (1). The p -values less than 0.001 were considered significant.

2.10. Examining temporal frequency of spatiotemporal patterns

In the following analyses, we used the simulated brain activities at $\kappa = 80$ and $v = 10$ m/s because they included multiple frequency components and the patterns' amplitudes estimated from the simulated brain activities resembled those estimated from the real data.

We examined the temporal frequency of the spatiotemporal patterns in the same way as with the real data (Section 2.6). First, we decomposed simulated brain activities $\sin(\theta_a)$ into the delta (0.4–4 Hz), theta (4–8 Hz), alpha (8–13 Hz), beta (13–30 Hz), and gamma (30–50 Hz) band components using FIR filters. Second, from the simulated brain activities in each band, we estimated the spatiotemporal patterns using the estimated onsets. Finally, we calculated their powers by averaging the squares of the patterns across the times and the ROIs.

To check whether the powers were larger than those generated from the fluctuations that were not time-locked to the estimated onsets, we compared the powers with surrogates. The surrogate powers were generated by randomly shuffling the IOIs of the estimated onsets and estimating the spatiotemporal patterns using the IOI-shuffled onsets.

2.11. Examining generating mechanism of spatiotemporal pattern

To examine how the spatiotemporal pattern was generated from the simulated brain activity ($\kappa = 80$ and $v = 10$ m/s), we calculated the phase-locking factors (PLFs) (Naruse et al., 2010; Tallon-Baudry et al., 1996) from the simulated brain activity after the estimated onsets. The PLFs were calculated by

$$l_a(t) = \left| \frac{1}{O} \sum_{o=1}^O \exp(i\theta_a(t - \tau_o + 1)) \right|,$$

where O is the number of estimated onsets and τ_o is the o -th onset time. This value becomes 1 if phase $\theta_a(t)$ was completely time-locked to the estimated onsets and close to 0 if it was time-unlocked.

2.12. Data and code availability

The processed data, such as the spatiotemporal patterns, are available from the authors upon request. The codes for estimating the source currents are available from https://vbmeg.atr.jp/docs/v22/static/vbmeg2_resting_state_tutorial.html. The codes for performing BigSTeP are available from <https://bicr.atr.jp/~takeda/BigSTeP.html>. The codes for simulating the brain activities are available from the authors upon request.

3. Results

3.1. Estimating repetitive spatiotemporal patterns

From the resting-state MEG and EEG data, we estimated the source currents by the LCMV beamformer (Van Veen et al., 1997) and normalized them to have mean 0 and SD 1 for each vertex. We verified the

Pattern 1 (Subject 10)

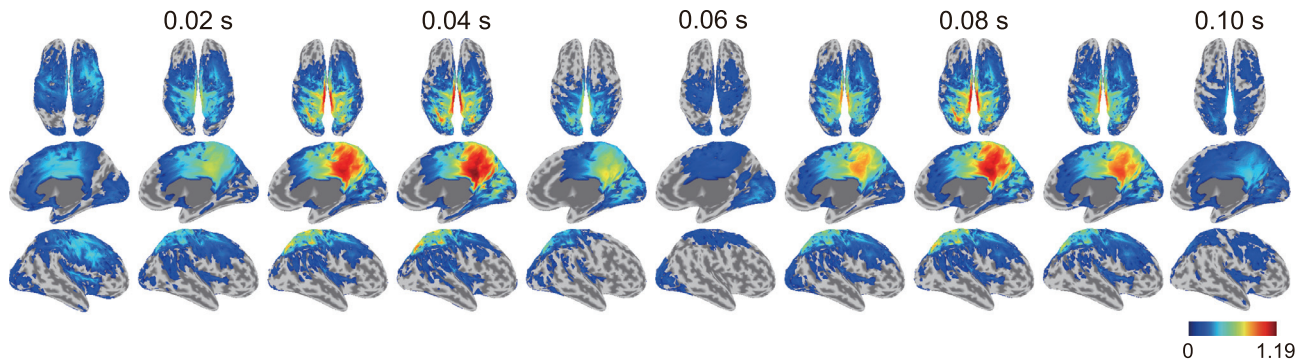


Fig. 2. Sample spatiotemporal pattern. Absolute values of subject 10's spatiotemporal pattern (patterns 1) is shown. Activities over 0.1 of their maximum value are shown.

estimated source currents by displaying the spatial distributions of their powers (Supplementary material, SFig. 3B).

To extract the repetitive spatiotemporal patterns, we applied Big-STEP (Takeda et al., 2019a) to the source currents for each subject. The number and length of the patterns were determined based on the reproducibility of the estimated patterns. We separately estimated the patterns from the two runs, vectorized them, and calculated their correlation coefficients between runs. Fig. 1 shows the resultant correlation coefficients of subject 10. When the number and length of the patterns were set to 1 and 0.1 s, respectively, the correlation coefficients exhibited a maximum value of 0.94. Therefore, we set the number and length of the patterns to these values for this subject. The correlation coefficients of all the subjects are shown in Supplementary material, SFig. 4. For all the subjects, the numbers were set to 1–3 and the lengths were set to 0.1–0.3 s.

Fig. 2 shows the estimated spatiotemporal pattern of subject 10 (pattern 1). Within 0.1 s, the activities globally and consecutively changed with time (Video 17). All the subjects' spatiotemporal patterns are shown in Videos 1–19. The numbers of onsets per second were 6.45 ± 2.27 , indicating that on average each pattern appeared about six times a second.

3.2. Spatiotemporal patterns were broadband

To examine which frequency component the estimated spatiotemporal patterns consisted of, we decomposed the patterns into the delta (0.4–4 Hz), theta (4–8 Hz), alpha (8–13 Hz), beta (13–30 Hz), and gamma (30–50 Hz) band components, and calculated their powers. To check whether the powers were larger than those generated from the fluctuations that were not time-locked to the estimated onsets, we compared the powers with the surrogates generated by the IOI-shuffled onsets.

Fig. 3A shows the resultant powers averaged across the times, vertices, patterns, and subjects. For all the bands, the original powers (blue line) were significantly larger than the surrogate ones (red line), indicating that for all the bands the spatiotemporal patterns had larger powers than the inherent fluctuations in the source currents. That is, the patterns were broadband. Fig. 3B shows the spatial distributions of the powers averaged across the times, patterns, and subjects. The powers were large around the cingulate cortex. A similar result with Fig. 3 was obtained from other hyperparameter values (Supplementary material, SFig. 5), indicating its robustness.

3.3. RSNs in spatiotemporal patterns

We next evaluated the spatial similarity between the spatiotemporal patterns and the fMRI-RSNs, which have been extensively examined in

human resting-state studies (Biswal et al., 1995; Fox et al., 2005; Raichle et al., 2001; Smith et al., 2009). For each frequency component of the patterns, we calculated the correlation coefficients between the patterns' absolute values at each time and the spatial patterns of the RSNs.

Fig. 4A shows the correlation coefficients for pattern 1 (subject 10) shown in Fig. 2. In each frequency component, pattern 1 transiently exhibited spatial patterns that significantly resembled the RSNs ($q < 0.01$). For example, the beta component exhibited spatial patterns that highly correlated with the visual 1, default mode and sensorimotor networks ($q < 0.01$). Note that the correlation coefficients seem to oscillate twice around each frequency band because they were calculated from the patterns' absolute values.

We summarized the results of all the subjects by examining how frequently high correlation coefficients were observed. Fig. 4B shows the proportions of the high correlation coefficients ($p < 0.01$) among all the times, patterns, and subjects. The theta, alpha and beta components frequently exhibited spatial patterns that highly correlated with the default mode and the sensorimotor networks. A similar result with Fig. 4B was obtained from other hyperparameter values (Supplementary material, SFig. 6), indicating its robustness.

These results suggest that multiple fMRI-RSNs were embedded in the multiple frequency components of the spatiotemporal patterns.

3.4. Simulation test

Using simulated brain activities, we examined how propagating activities along the anatomical connectivity formed such broadband spatiotemporal patterns. We assumed a whole-brain network model of Kuramoto oscillators [Eq. (2)] (Cabral et al., 2014; Gollo et al., 2017; Pang et al., 2021). The natural frequency, coupling strength, and delay between the ROIs were determined based on the anatomical connectivity.

We first characterized the behavior of the simulated brain activities by the synchrony degree [Eq. (3)] (Cabral et al., 2014), which quantifies the phase consistency across the ROIs. Fig. 5A shows the temporal means (left) and SDs (right) of the synchrony degrees. They changed depending on the following parameters: global coupling strength [κ in Eq. (2)] and conduction velocity, which determined the delays across the ROIs [τ_{ab} in Eq. (2)]. The SD (Fig. 5A, right) captures how largely the synchrony degrees fluctuated in time and indicates the system's metastability level (Cabral et al., 2014).

We also examined the width of the frequency band in the simulated brain activity by calculating the entropy of their peak frequencies (Fig. 5B). The entropies decreased as the global coupling strength increased (Fig. 5B), indicating that the bandwidth narrowed as the coupling strength increased.

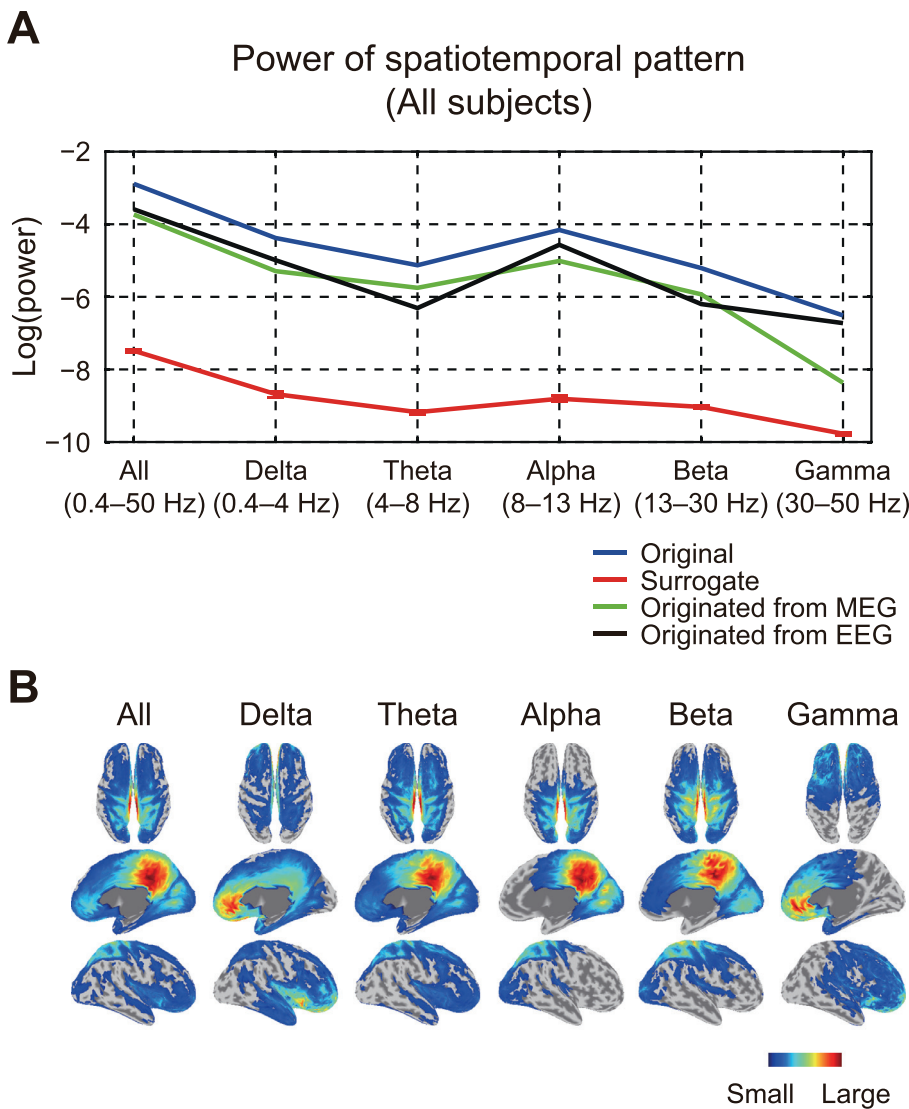


Fig. 3. Temporal frequency of spatiotemporal patterns. (A) Power of spatiotemporal patterns in each frequency component. Powers averaged across times, vertices, patterns, and subjects are shown. Error bars of red line represent SDs of surrogate powers across 1,000 repeats. (B) Spatial distribution of spatiotemporal patterns' powers in each frequency component. Powers were averaged across times, patterns, and subjects. For each frequency component, powers over 0.1 of their maximum value are shown.

For each parameter pair, we estimated the repetitive spatiotemporal patterns from the simulated brain activities. Although the simulated brain activities had many differences from the real ones owing to the model's simplicity, we expected that the patterns estimated from the simulated and real data had common characteristics if both reflected the propagating activities along the human brains' connectivity. To test this expectation, we compared the patterns of the simulated and real data. Because the patterns that were estimated from the real data shared a tendency in their amplitudes across the subjects (Fig. 3B and Supplementary material, SFig. 2), we characterized the patterns by their amplitudes. Fig. 5C shows the correlation coefficients of the patterns' amplitudes between the simulated and real data. In a wide range of parameters, the correlation coefficients were significantly high ($p < 0.001$), suggesting the validity of our expectation. The correlation coefficients especially tended to be high as the metastability level increased (their correlation coefficient was 0.53, $p < 0.001$) (Fig. 5A right and C). Indeed, where the global coupling strength = 80 and the conduction velocity = 10 m/s, which exhibited a high metastability level (Fig. 5A, right), the pattern estimated from the simulated data had a large amplitude around the cingulate cortex (Fig. 5D) like those estimated from the real data (Fig. 3B). These results suggest that the patterns estimated from the real data reflected the propagating activities in the metastable brain dynamics.

To examine the generating mechanism of the broadband spatiotemporal patterns estimated from real data (Fig. 3A), we chose the simu-

lated brain activities at global coupling strength = 80 and conduction velocity = 10 m/s. At these parameter values, the simulated brain activities included multiple frequency components (Fig. 5B) and the patterns' amplitudes were similar between the simulated and real data (Fig. 5C).

Fig. 6A shows the power of the spatiotemporal patterns estimated from the simulated brain activities at each frequency band. For the alpha, beta, and gamma bands, they were significantly larger than the surrogates (red line), indicating that for these bands the spatiotemporal patterns had larger powers than the inherent fluctuations in the simulated brain activities. That is, the patterns consisted of alpha, beta, and gamma band components.

We further chose three ROIs (R_V1_ROI, L_10d_ROI, and R_v23ab_ROI) at which the patterns had large amplitudes in the alpha, beta, and gamma bands, respectively. Fig. 6B shows the patterns at these ROIs. Their amplitudes were significantly larger than the surrogate ones generated by the IOI-shuffled onsets. To identify the factor responsible for the large amplitudes, we displayed phases $\theta_a(t)$ after the estimated onsets in Fig. 6C. They seem consistent across the onsets when the pattern exhibited large amplitudes (e.g., around 0.08 s for R_V1_ROI, Fig. 6B and C). Indeed, the PLFs, which quantify the phase consistencies across the onsets, became high at these times (Fig. 6B and D). These results indicate that the phase consistency across the onsets increased the pattern's amplitudes as with the stimulus-triggered averages (Makeig et al., 2002). We believe that the propagating activity aligned the phases of the alpha, beta, and gamma band oscillators at

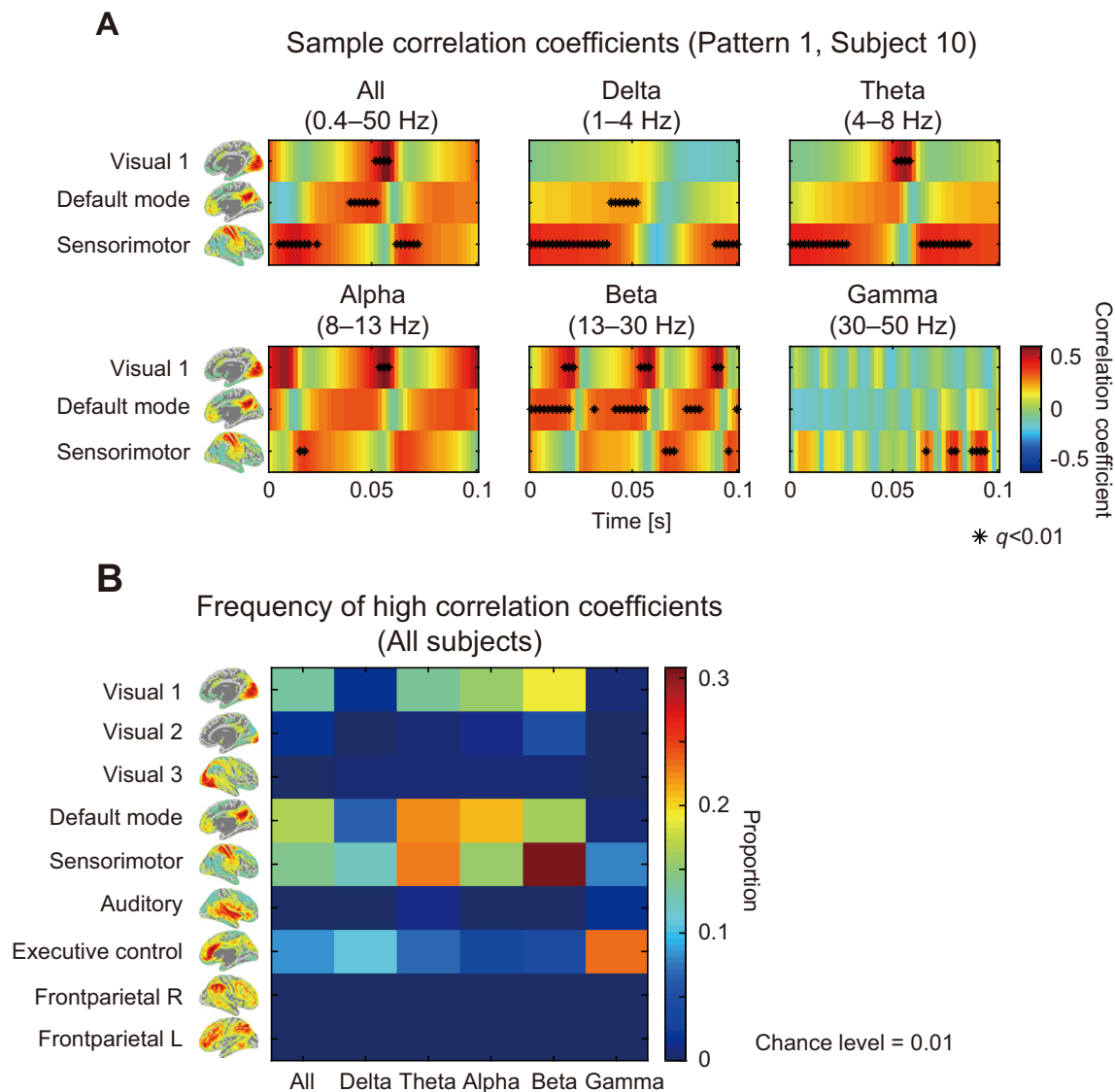


Fig. 4. Spatial similarity between spatiotemporal patterns and fMRI-RSNs. (A) Sample correlation coefficients between pattern 1 (subject 10) and fMRI-RSNs. RSNS are shown which exhibited significant ($q < 0.01$) and high ($r > 0.3$) correlation coefficients. (B) Frequency of high correlation coefficients. Proportions of high correlation coefficients ($p < 0.01$) among all the times, patterns, and subjects are shown. Chance level was 0.01.

these ROIs, and their phase consistencies across the onsets increased, resulting in large amplitudes at these ROIs and bands.

4. Discussion

In this study, we identified the repetitive spatiotemporal patterns from the resting-state brain activities estimated from MEG and EEG data. The patterns consisted of multiple frequency components, each of which transiently exhibited the frequency-specific RSNS. The simulation test suggests that the patterns reflected the phase alignment of the multiple frequency oscillators induced by the propagating activities along the anatomical connectivity. These results revealed whole-brain propagating activities that transiently exhibited multiple fMRI-RSNS in their multiple frequency components.

4.1. Reliability of spatiotemporal patterns

Using BigSTeP, we estimated the repetitive spatiotemporal patterns from the resting-state brain activities. Although perhaps such repetitive patterns do not exist and those shown in our study (Fig. 2) simply reflect

the random fluctuations inherent in the resting-state brain activities, we believe this possibility is unlikely for the following three reasons. First, many experimental (Han et al., 2008; Ikegaya et al., 2004; Ji and Wilson, 2007; Matsui et al., 2016; Wilson and McNaughton, 1994) and theoretical (Izhikevich et al., 2004; Roberts et al., 2019; Teramae et al., 2012) studies have reported the emergence of repetitive spatiotemporal patterns in resting-state brain activities. Therefore, it is reasonable that our data also exhibited such patterns that were extracted by BigSTeP. Second, the estimated patterns had high reproducibility between the two runs (Fig. 1 and Supplementary material, SFig. 4). If the patterns reflected random fluctuations, the reproducibility would be much lower. Finally, the powers of the patterns were significantly larger than the surrogate ones, which were generated using IOI-shuffled onsets (Fig. 3A). This result indicates that the patterns were not generated from fluctuations time-unlocked to the estimated onsets.

4.2. Generating mechanism of spatiotemporal patterns

To gain insight into the generating mechanism of broadband spatiotemporal patterns (Fig. 3A), we conducted a simulation test (Figs. 5

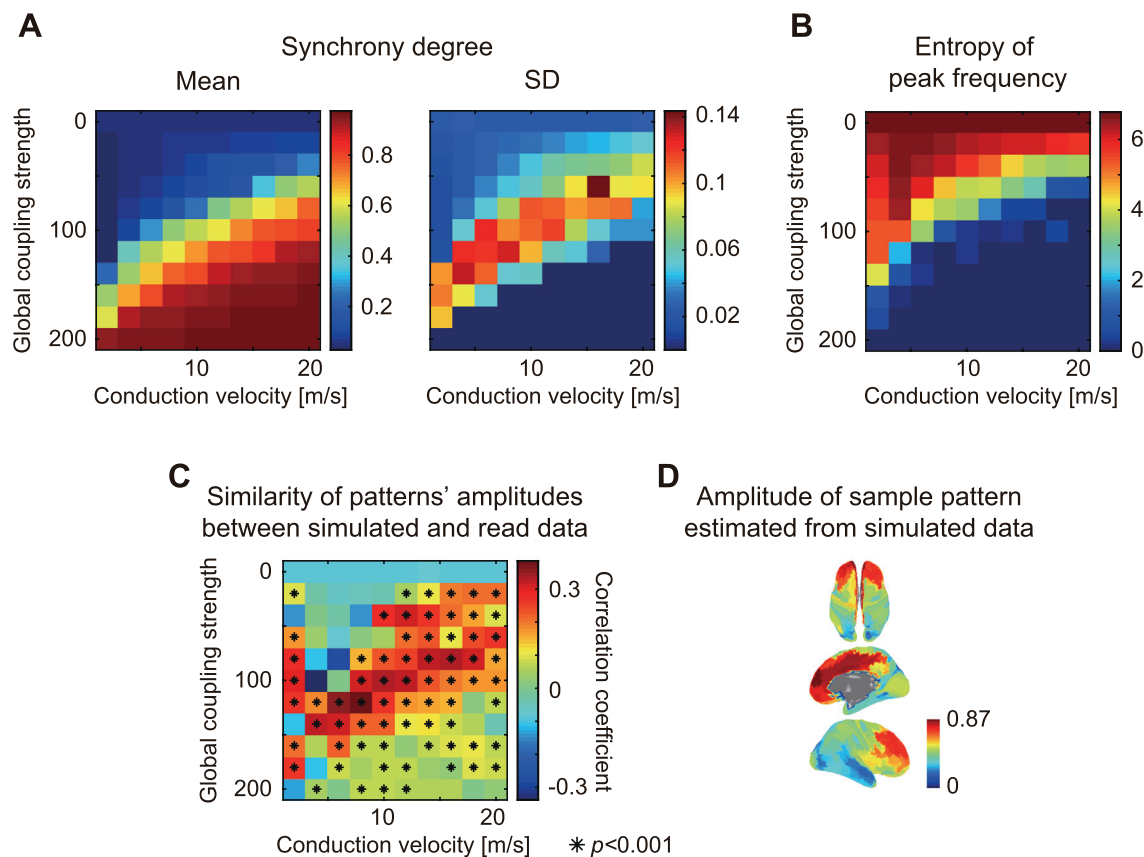


Fig. 5. Behavior of simulated brain activities. (A) Synchrony degree. Left and right figures show temporal mean and SD of synchrony degrees. (B) Entropy of peak frequencies. (C) Similarity of spatiotemporal patterns estimated from simulated and real data. Correlation coefficients of patterns' amplitudes are shown between simulated and real data. Correlation coefficients were averaged across iterations. (D) Amplitude of sample pattern estimated from simulated data at global coupling strength = 80 and conduction velocity = 10 m/s.

and 6). Using the whole-brain network model of the Kuramoto oscillators, we examined how the propagating activity along the anatomical connectivity formed a broadband spatiotemporal pattern. It was shown that the phase consistency across the estimated onsets increased the pattern's amplitudes in the multiple frequency bands (Fig. 6B and D).

About two decades ago, Makeig et al. (2002) showed that event-related potentials were mainly generated by stimulus-induced phase resetting of ongoing rhythms. More specifically, the stimulus-induced propagating activities modulated the phases of oscillators to fixed values at fixed times after the stimulus onsets, and the stimulus-triggered averaging procedure enhanced such stimulus-locked phases. Likewise in our case, the internally-induced propagating activities probably modulated the phases of the multiple frequency oscillators to fixed values at fixed times after the estimated onsets, and their phase consistencies across the onsets increased, resulting in broadband spatiotemporal patterns (Fig. 3A).

On the other hand, the similarity of the patterns' amplitudes estimated from the simulated and real data tended to be higher as the metastability level increased (Fig. 5A right and C). Metastability is a dynamical phenomenon, in which the system's state spontaneously cycles between multiple weakly attracting states (Heitmann and Breakpear, 2018; Sase and Kitajo, 2021), and might account for the dynamics of spontaneous brain activities (Roberts et al., 2019; Sase and Kitajo, 2021). Our result suggests that the spatiotemporal patterns reflected the fixed paths that the states repeatedly went through in the metastable brain dynamics.

In this simulation test, we used the simple model and focused on the phase dynamics of limit-cycle oscillators coupled across the 360 ROIs while ignoring their amplitudes. On the other hand, more detailed mod-

els have been proposed, such as the neural mass model (Jansen and Rit, 1995). Adopting such detailed models might reproduce various characteristics of spatiotemporal patterns, such as the power spectrum (Fig. 3A).

4.3. Relationship between neuronal propagating activities and hemodynamic RSNs

Matsui et al. (2016) simultaneously recorded neuronal calcium and hemodynamic signals from mouse cortices and found that the hemodynamic RSNs were embedded in the phases of neuronal propagating activities. Our results extended this finding for human subjects. We revealed the whole-brain propagating activities from the resting-state MEG and EEG data. They transiently exhibited multiple RSNs in their multiple frequency components (Fig. 4). Human resting-state fMRIs have been shown to include various RSNs (Smith et al., 2009). Such variability may be partially attributable to the various frequency components in the neuronal propagating activities.

Connectome harmonics, which is the Laplacian eigenvectors of the anatomical connectivity derived from dmRI, characterizes how activity is diffused along the connectivity. Connectome harmonics resembles the spatial patterns of the fMRI-RSNs (Atasoy et al., 2016), suggesting that the neuronal propagating activities along the anatomical connectivity contribute to fMRI-RSNs. In our study, we showed that the propagating activities estimated from the resting-state MEG and EEG data transiently exhibited spatial patterns resembling fMRI-RSNs (Fig. 4). Therefore, our results demonstrated the validity of the suggestion from connectome harmonics.

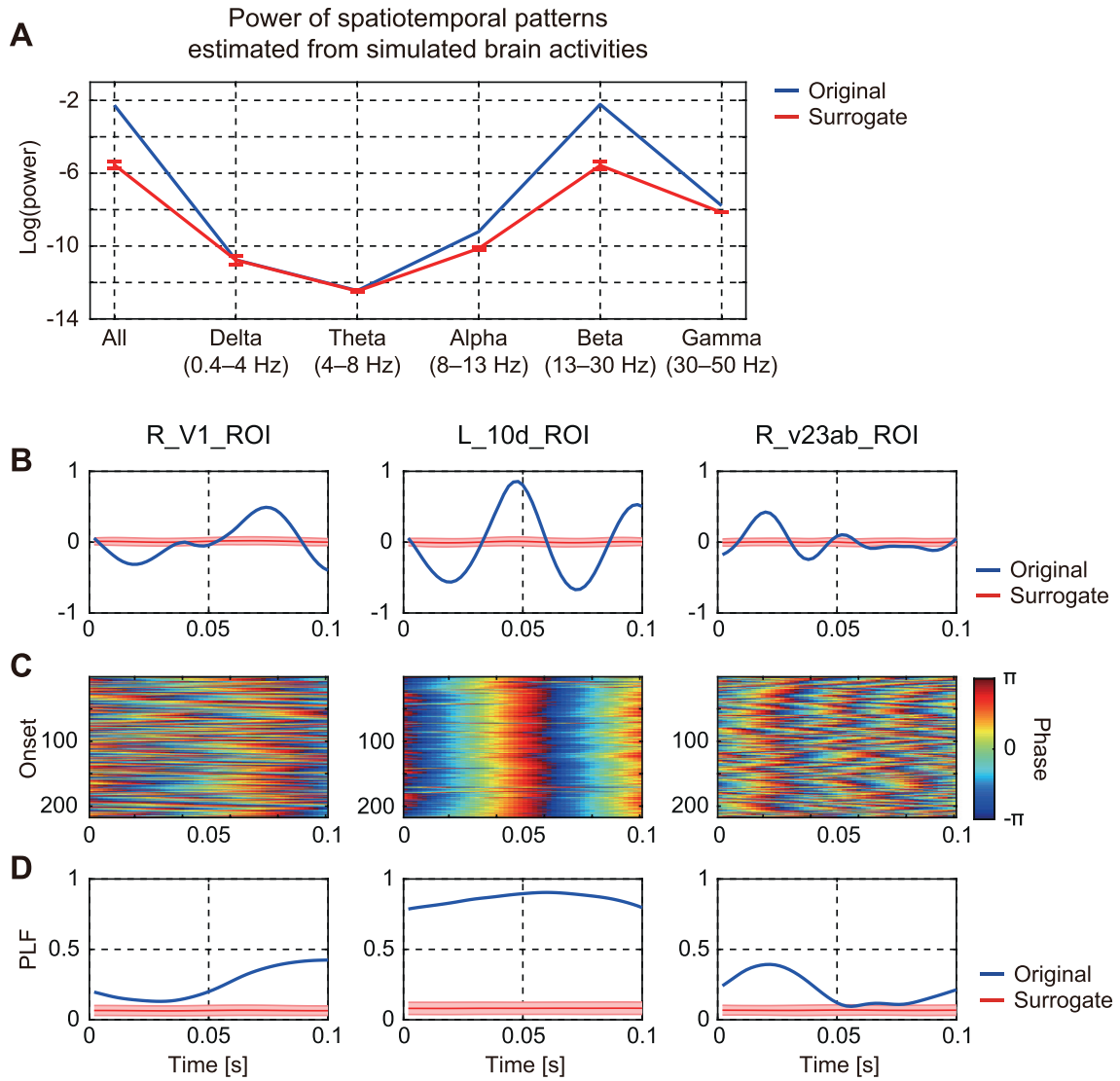


Fig. 6. Detailed properties of simulated brain activities at global coupling strength = 80 and conduction velocity = 10 m/s. (A) Power of spatiotemporal patterns estimated from simulated brain activities. Powers averaged across times and iterations are shown for each frequency component. Error bars of red line represent SDs of surrogate powers across 1,000 repeats. (B) Sample pattern at three ROIs (R_V1_ROI, L_10d_ROI, and R_v23ab_ROI), which respectively included large alpha, beta, and gamma band components. Red lines and areas show means and SDs of surrogate patterns across 1,000 repeats. (C) Phases after estimated onsets. (D) Phase-locking factors (PLFs). Red lines and areas show means and SDs of surrogate PLFs across 1,000 repeats.

4.4. Necessity to use both MEG and EEG data

Previous human EEG studies suggested the existence of whole-brain propagating activities in a resting-state (Ito et al., 2005; 2007; Massimini et al., 2004). However, because these works did not estimate the source currents, their detailed locations are unclear. Generally speaking, estimating source currents only from EEG is difficult owing to its low spatial resolution. In this study, we reduced this difficulty by integrating MEG with the EEG data. Because these measurements have different sensitivities to source currents, integrating them alleviates the ill-posed nature of MEG/EEG source imaging (Takeda et al., 2019b). Indeed, we obtained reliable source currents (Supplementary material, SFig. 3B) that are consistent with a previous MEG study (Niso et al., 2019).

Furthermore, the MEG and EEG data almost equally contributed to generating the spatiotemporal patterns (Fig. 3A). This also indicates the necessity of using both MEG and EEG data to identify the whole-brain propagating activities in the source space.

4.5. Relation to other resting-state MEG/EEG studies

Using cluster analyses and hidden Markov models (HMMs), MEG/EEG studies have characterized resting-state MEG/EEG data by segmenting them into a few representative states (e.g., microstates) (Baker et al., 2014; Michel and Koenig, 2018; Pascual-Marqui et al., 1995; Vidaurre et al., 2018; Woolrich et al., 2013). In contrast, we estimated the repetitive spatiotemporal patterns to capture the propagating activities. If an activity propagates across different regions (e.g., from visual to motor cortices), its spatial pattern consecutively changes with time. BigSTeP can represent it with a spatiotemporal pattern while cluster analyses and HMMs reduce it to a state or a state transition. Therefore, BigSTeP is suitable for our purpose.

The spatiotemporal patterns included multiple frequency components (Fig. 3A), indicating that the phases were time-locked across the frequencies in the patterns. On the other hand, MEG/EEG studies reported cross-frequency phase synchronization (Baselice et al., 2019; Palva and Palva, 2018; Sorrentino et al., 2020), where the phases of

a frequency band are time-locked to those of another frequency band. Our result suggests that cross-frequency phase synchronization is at least partially attributable to whole-brain propagating activities.

The spatiotemporal patterns transiently exhibited multiple fMRI-RSNs in their multiple frequency components. For example, the alpha component exhibited the default mode and sensorimotor networks, and the beta component exhibited sensorimotor networks (Fig. 4). This result is consistent with a previous EEG-fMRI study that examined the correlation between the fluctuation of fMRI-RSNs and the concurrent EEG powers (Mantini et al., 2007). They found that the DMN fluctuation highly correlated with the EEG powers in the alpha and beta bands and the sensorimotor network's fluctuation highly correlated with the EEG power in the beta band.

4.6. Functional role of whole-brain propagating activities

The existence of multiple frequency components and RSNs in a spatiotemporal pattern indicates that they appeared in a time-locked way, implying the information transmission across these activities. This suggests that the patterns reflect a process that integrates the information distributed over the frequencies and networks to generate consciousness. Indeed, the patterns' lengths (0.1–0.3 s) were almost consistent with a suggested timescale of consciousness (around 0.2 s) (Deco et al., 2019), and the patterns had large powers around the posterior cingulate cortex (Fig. 3B), whose activities reduced in unconscious states (Dehaene and Changeux, 2011). Furthermore, propagating activities in awake states were shown to contribute to cognitive functions (Davis et al., 2020; Zhang et al., 2018). Therefore, further investigation of the whole-brain propagating activities may elucidate the mechanism of consciousness.

Declaration of Competing Interest

The authors declare no competing interest.

Credit authorship contribution statement

Yusuke Takeda: Conceptualization, Formal analysis, Funding acquisition, Project administration, Investigation, Methodology, Software, Validation, Visualization, Writing – original draft, Writing – review & editing. **Nobuo Hiroe:** Conceptualization, Data curation, Investigation, Writing – review & editing. **Okito Yamashita:** Conceptualization, Funding acquisition, Project administration, Resources, Supervision, Writing – review & editing.

Acknowledgments

This research was supported by a contract with the National Institute of Information and Communications Technology entitled “Analysis of multi-modal brain measurement data and development of its application for BMI open innovation” (209). This research was also supported by the Japan Agency for Medical Research and Development (AMED) (Grant Number JP20dm0307009) and Japan Society for the Promotion of Science (JSPS) KAKENHI (Grant Number 21K07269, 20H00600).

Supplementary material

Supplementary material associated with this article can be found, in the online version, at [10.1016/j.neuroimage.2021.118711](https://doi.org/10.1016/j.neuroimage.2021.118711).

References

Atasoy, S., Donnelly, I., Pearson, J., 2016. Human brain networks function in connectome-specific harmonic waves. *Nat. Commun.* 7, 10340. doi:10.1038/ncomms10340.
Baker, A.P., Brookes, M.J., Rezek, I.A., Smith, S.M., Behrens, T., Smith, P.J.P., Woolrich, M., 2014. Fast transient networks in spontaneous human brain activity. *Elife* 3, e01867. doi:10.7554/eLife.01867.

Basti, A., Chella, F., Snyder, A.Z., Pizzella, V., Marzetti, L., 2019. Spatiotemporal structures of time lags in the brain as revealed by magnetoencephalography. In: Proceedings of the IEEE International Conference on Systems, Man and Cybernetics (SMC), pp. 2762–2766. doi:10.1109/SMC.2019.8914571.
Benjamini, Y., Hochberg, Y., 1995. Controlling the false discovery rate: a practical and powerful approach to multiple testing. *J. R. Stat. Soc. Ser. B Stat. Methodol.* 57, 289–300.
Biswal, B.B., Yetkin, F.Z., Haughton, V.M., Hyde, J.S., 1995. Functional connectivity in the motor cortex of resting human brain using echo-planar MRI. *Magn. Reson. Med.* 34, 537–541. doi:10.1002/mrm.1910340409.
Brookes, M.J., Woolrich, M.W., Barnes, G.R., 2012. Measuring functional connectivity in MEG: a multivariate approach insensitive to linear source leakage. *Neuroimage* 63, 910–920. doi:10.1016/j.neuroimage.2012.03.048.
Cabral, J., Luckhoo, H., Woolrich, M., Joensson, M., Mohseni, H., Baker, A., Kringelbach, M.L., Deco, G., 2014. Exploring mechanisms of spontaneous functional connectivity in MEG: how delayed network interactions lead to structured amplitude envelopes of band-pass filtered oscillations. *Neuroimage* 90, 423–435. doi:10.1016/j.neuroimage.2013.11.047.
de Cheveigné, A., Simon, J.Z., 2007. Denoising based on time-shift PCA. *J. Neurosci. Methods* 165, 297–305. doi:10.1016/j.jneumeth.2007.06.003.
Colclough, G.L., Brookes, M.J., Smith, S.M., Woolrich, M.W., 2015. A symmetric multivariate leakage correction for MEG connectomes. *Neuroimage* 117, 439–448. doi:10.1016/j.neuroimage.2015.03.071.
Davis, Z.W., Muller, L., Martinez-Trujillo, J., Sejnowski, T., Reynolds, J.H., 2020. Spontaneous travelling cortical waves gate perception in behaving primates. *Nature* 587, 432–436. doi:10.1038/s41586-020-2802-y.
Deco, G., Cruzat, J., Kringelbach, M.L., 2019. Brain songs framework used for discovering the relevant timescale of the human brain. *Nat. Commun.* 10, 583. doi:10.1038/s41467-018-08186-7.
Dehaene, S., Changeux, J.P., 2011. Experimental and theoretical approaches to conscious processing. *Neuron* 70, 200–227. doi:10.1016/j.neuron.2011.03.018.
Dragoi, G., Tonegawa, S., 2011. Preplay of future place cell sequences by hippocampal cellular assemblies. *Nature* 469, 397–401. doi:10.1038/nature09633.
Baselice, F., Sorriso, A., Rucco, R., Sorrentino, P., 2019. Phase linearity measurement: a novel index for brain functional connectivity. *IEEE Trans. Med. Imaging* 38, 873–882. doi:10.1109/TMI.2018.2873423.
Fox, M.D., Snyder, A.Z., Vincent, J.L., Corbetta, M., Van Essen, D.C., Raichle, M.E., 2005. The human brain is intrinsically organized into dynamic, anticorrelated functional networks. *Proc. Natl. Acad. Sci. U.S.A.* 102, 9673–9678. doi:10.1073/pnas.0504136102.
Glasser, M.F., Coalson, T.S., Robinson, E.C., Hacker, C.D., Harwell, J., Yacoub, E., Ugurbil, K., Andersson, J., Beckmann, C.F., Jenkinson, M., Smith, S.M., Van Essen, D.C., 2016. A multi-modal parcellation of human cerebral cortex. *Nature* 536, 171–178. doi:10.1038/nature18933.
Gollo, L.L., Roberts, J.A., Cocchi, L., 2017. Mapping how local perturbations influence systems-level brain dynamics. *Neuroimage* 160, 97–112. doi:10.1016/j.neuroimage.2017.01.057.
Han, F., Caporale, N., Dan, Y., 2008. Reverberation of recent visual experience in spontaneous cortical waves. *Neuron* 60, 321–327. doi:10.1016/j.neuron.2008.08.026.
Heitmann, S., Breakspear, M., 2018. Putting the “dynamic” back into dynamic functional connectivity. *Netw. Neurosci.* 2 (2), 150–174. doi:10.1162/netn_a_00041.
Henson, R.N., Wakeman, D.G., Litvak, V., Friston, K.J., 2011. A parametric empirical Bayesian framework for the EEG/MEG inverse problem: generative models for multi-subject and multi-modal integration. *Front. Hum. Neurosci.* 5, 76. doi:10.3389/fnhum.2011.00076.
Ikegaya, Y., Aaron, G., Cossart, R., Aronov, D., Lampl, I., Ferster, D., Yuste, R., 2004. Synfire chains and cortical songs: temporal modules of cortical activity. *Science* 304, 559–564. doi:10.1126/science.1093173.
Ito, J., Nikolaev, A.R., Van Leeuwen, C., 2005. Spatial and temporal structure of phase synchronization of spontaneous alpha EEG activity. *Biol. Cybern.* 92, 54–60. doi:10.1007/s00422-004-0533-z.
Ito, J., Nikolaev, A. R., Van Leeuwen, C., 2007. Dynamics of spontaneous transitions between global brain states. *Hum. Brain Mapp.* 28, 904–913. doi:10.1002/hbm.20316.
Izhikevich, E.M., Gally, J.A., Edelman, G.M., 2004. Spike-timing dynamics of neuronal groups. *Cereb. Cortex* 14, 933–944. doi:10.1093/cercor/bhh053.
Jansen, B.H., Rit, V.G., 1995. Electroencephalogram and visual evoked potential generation in a mathematical model of coupled cortical columns. *Biol. Cybern.* 73, 357–366. doi:10.1007/bf00199471.
Ji, D., Wilson, M. A., 2007. Coordinated memory replay in the visual cortex and hippocampus during sleep. *Nat. Neurosci.* 10, 100–107. doi:10.1038/nn1825.
Jung, T.P., Makeig, S., Westerfield, M., Townsend, J., Courchesne, E., Sejnowski, T.J., 2001. Analysis and visualization of single-trial event-related potentials. *Hum. Brain Mapp.* 14, 166–185. doi:10.1002/hbm.1050.
Majeed, W., Magnuson, M., Hasenkamp, W., Schwarb, H., Schumacher, E.H., Barsalou, L., Keilholz, S.D., 2011. Spatiotemporal dynamics of low frequency BOLD fluctuations in rats and humans. *Neuroimage* 54, 1140–1150. doi:10.1016/j.neuroimage.2010.08.030.
Makeig, S., Westerfield, M., Jung, T.P., Enghoff, S., Townsend, J., Courchesne, E., Sejnowski, T.J., 2002. Dynamic brain sources of visual evoked responses. *Science* 295, 690–694. doi:10.1126/science.1066168.
Mantini, D., Perrucci, M.G., Del Gratta, C., Romani, G.L., Corbetta, M., 2007. Electrophysiological signatures of resting state networks in the human brain. *Proc. Natl. Acad. Sci. U.S.A.* 104, 13170–13175. doi:10.1073/pnas.0700668104.
Massimini, M., Huber, R., Ferrarelli, F., Hill, S., Tononi, G., 2004. The sleep slow oscillation as a traveling wave. *J. Neurosci.* 24, 6862–6870. doi:10.1523/jneurosci.1318-04.2004.

- Matsui, T., Murakami, T., Ohki, K., 2016. Transient neuronal coactivations embedded in globally propagating waves underlie resting-state functional connectivity. *Proc. Natl. Acad. Sci. U.S.A.* 113, 6556–6561. doi:10.1073/pnas.1521299113.
- Michel, C.M., Koenig, T., 2018. EEG microstates as a tool for studying the temporal dynamics of whole-brain neuronal networks: a review. *Neuroimage* 180, 577–593. doi:10.1016/j.neuroimage.2017.11.062.
- Mitra, A., Raichle, M.E., 2016. How networks communicate: propagation patterns in spontaneous brain activity. *Philos. Trans. R. Soc. Lond. B Biol. Sci.* 371, 20150546. doi:10.1098/rstb.2015.0546.
- Mitra, A., Snyder, A.Z., Blazey, T., Raichle, M.E., 2015a. Lag threads organize the Brain's intrinsic activity. *Proc. Natl. Acad. Sci. U.S.A.* 112, E2235–E2244. doi:10.1073/pnas.1503960112.
- Mitra, A., Snyder, A.Z., Hacker, C.D., Raichle, M.E., 2014. Lag structure in resting-state fMRI. *J. Neurophysiol.* 111, 2374–2391. doi:10.1152/jn.00804.2013.
- Mitra, A., Snyder, A.Z., Tagliazucchi, E., Laufs, H., Raichle, M.E., 2015b. Propagated infraslow intrinsic brain activity reorganizes across wake and slow wave sleep. *Elife* 4, e10781. doi:10.7554/eLife.10781.
- Muller, L., Chavane, F., Reynolds, J., Sejnowski, T.J., 2018. Cortical travelling waves: mechanisms and computational principles. *Nat. Rev. Neurosci.* 19, 255–268. doi:10.1038/nrn.2018.20.
- Muller, L., Piantoni, G., Koller, D., Cash, S.S., Halgren, E., Sejnowski, T.J., 2016. Rotating waves during human sleep spindles organize global patterns of activity that repeat precisely through the night. *Elife* 5, e17267. doi:10.7554/eLife.17267.
- Naruse, Y., Matani, A., Miyawaki, Y., Okada, M., 2010. Influence of coherence between multiple cortical columns on alpha rhythm: a computational modeling study. *Hum. Brain Mapp.* 31, 703–715. doi:10.1002/hbm.20899.
- Niso, G., Tadel, F., Bock, E., Cousineau, M., Santos, A., Baillet, S., 2019. Brainstorm pipeline analysis of resting-state data from the open MEG archive. 284, 10.3389/fnins.2019.00284, *Front. Neurosci.* 13.
- Okazaki, Y.O., Nakagawa, Y., Mizuno, Y., Hanakawa, T., Kitajo, K., 2021. Frequency- and area-specific phase entrainment of intrinsic cortical oscillations by repetitive transcranial magnetic stimulation. *Front. Hum. Neurosci.* 15, 608947. doi:10.3389/fnhum.2021.608947.
- Palva, J.M., Palva, S., 2018. Functional integration across oscillation frequencies by cross-frequency phase synchronization. *Eur. J. Neurosci.* 48, 2399–2406. doi:10.1111/ejn.13767.
- Pang, J.C., Gollo, L.L., Roberts, J.A., 2021. Stochastic synchronization of dynamics on the human connectome. *Neuroimage* 229, 117738. doi:10.1016/j.neuroimage.2021.117738.
- Pascual-Marqui, R.D., Michel, C.M., Lehmann, D., 1995. Segmentation of brain electrical activity into microstates: model estimation and validation. *IEEE Trans. Biomed. Eng.* 42, 658–665. doi:10.1109/10.391164.
- Raichle, M.E., MacLeod, A.M., Snyder, A.Z., Powers, W.J., Gusnard, D.A., Shulman, G.L., 2001. A default mode of brain function. *Proc. Natl. Acad. Sci. U.S.A.* 98, 676–682. doi:10.1073/pnas.98.2.676.
- Roberts, J.A., Gollo, L.L., Abeyururi, R.G., Roberts, G., Mitchell, P.B., Woolrich, M.W., Breakspear, M., 2019. Metastable brain waves. *Nat. Commun.* 10, 1056. doi:10.1038/s41467-019-08999-0.
- Rosanova, M., Casali, A., Bellina, V., Resta, F., Mariotti, M., Massimini, M., 2009. Natural frequencies of human corticothalamic circuits. *J. Neurosci.* 29, 7679–7685. doi:10.1523/jneurosci.0445-09.2009.
- Rosen, B.Q., Halgren, E., 2021. A whole-cortex probabilistic diffusion tractography connectome. *eNeuro* 8. doi:10.1523/eneuro.0416-20.2020.
- Sase, T., Kitajo, K., 2021. The metastable brain associated with autistic-like traits of typically developing individuals. *PLoS Comput. Biol.* 17, e1008929. doi:10.1371/journal.pcbi.1008929.
- Sato, M., Yamashita, O., Sato, M., Miyawaki, Y., 2018. Information spreading by a combination of MEG source estimation and multivariate pattern classification. *PLoS One* 13, e0198806. doi:10.1371/journal.pone.0198806.
- Sato, M., Yoshioka, T., Kajihara, S., Toyama, K., Goda, N., Doya, K., Kawato, M., 2004. Hierarchical Bayesian estimation for MEG inverse problem. *Neuroimage* 23, 806–826. doi:10.1016/j.neuroimage.2004.06.037.
- Smith, S.M., Fox, P.T., Miller, K.L., Glahn, D.C., Fox, P.M., Mackay, C.E., Filippini, N., Watkins, K.E., Toro, R., Laird, A.R., Beckmann, C.F., 2009. Correspondence of the brain's functional architecture during activation and rest. *Proc. Natl. Acad. Sci. U.S.A.* 106, 13040–13045. doi:10.1073/pnas.0905267106.
- Sorrentino, P., Ambrosanio, M., Rucco, R., Cabral, J., Gollo, L.L., Breakspear, M., Baseline, F., 2020. Detection of cross-frequency coupling between brain areas: an extension of phase-linearity measurement. *bioRxiv*. doi:10.1101/2020.11.25.398628.
- Storey, J.D., Tibshirani, R., 2003. Statistical significance for genomewide studies. *Proc. Natl. Acad. Sci. U.S.A.* 100, 9440–9445. doi:10.1073/pnas.1530509100.
- Takahashi, K., Saleh, M., Penn, R.D., Hatsopoulos, N., 2011. Propagating waves in human motor cortex. *Front. Hum. Neurosci.* 5. doi:10.3389/fnhum.2011.00040.
- Takeda, Y., Hiroe, N., Yamashita, O., Sato, M., 2016. Estimating repetitive spatiotemporal patterns from resting-state brain activity data. *Neuroimage* 133, 251–265. doi:10.1016/j.neuroimage.2016.03.014.
- Takeda, Y., Itahashi, T., Sato, M., Yamashita, O., 2019a. Estimating repetitive spatiotemporal patterns from many subjects' resting-state fMRIs. *Neuroimage* 203, 116182. doi:10.1016/j.neuroimage.2019.116182.
- Takeda, Y., Suzuki, K., Yamashita, O., Kawato, M., 2019b. MEG source imaging and group analysis using VBMEG. *Front. Neurosci.* 13. doi:10.3389/fnins.2019.00241.
- Tallon-Baudry, C., Bertrand, O., Delpuech, C., Pernier, J., 1996. Stimulus specificity of phase-locked and non-phase-locked 40 Hz visual responses in human. *J. Neurosci.* 16, 4240–4249. doi:10.1523/jneurosci.16-13-04240.1996.
- Teramae, J., Tsubo, Y., Fukai, T., 2012. Optimal spike-based communication in excitable networks with strong-sparse and weak-dense links. *Sci. Rep.* 2, 485. doi:10.1038/srep00485.
- Van Veen, B.D., van Drongelen, W., Yuchtman, M., Suzuki, A., 1997. Localization of brain electrical activity via linearly constrained minimum variance spatial filtering. *IEEE Trans. Biomed. Eng.* 44, 867–880. doi:10.1109/10.623056.
- Vidaurre, D., Hunt, L.T., Quinn, A.J., Hunt, B.A., Brookes, M.J., Nobre, A.C., Woolrich, M.W., 2018. Spontaneous cortical activity transiently organises into frequency specific phase-coupling networks. *Nat. Commun.* 9, 2987. doi:10.1038/s41467-018-05316-z.
- Wilson, M.A., McNaughton, B.L., 1994. Reactivation of hippocampal ensemble memories during sleep. *Science* 265, 676–679. doi:10.1126/science.8036517.
- Woolrich, M., Baker, A., Luckhoo, H., Mohseni, H., Barnes, G., Brookes, M., Rezek, I., 2013. Dynamic state allocation for MEG source reconstruction. *Neuroimage* 77, 77–92. doi:10.1016/j.neuroimage.2013.03.036.
- Yoshioka, T., Toyama, K., Kawato, M., Yamashita, O., Nishina, S., Yamagishi, N., Sato, M., 2008. Evaluation of hierarchical Bayesian method through retinotopic brain activities reconstruction from fMRI and MEG signals. *Neuroimage* 42, 1397–1413. doi:10.1016/j.neuroimage.2008.06.013.
- Zalesky, A., Fornito, A., Cocchi, L., Gollo, L.L., Breakspear, M., 2014. Time-resolved resting-state brain networks. *Proc. Natl. Acad. Sci. U.S.A.* 111, 10341–10346. doi:10.1073/pnas.1400181111.
- Zhang, H., Watrous, A.J., Patel, A., Jacobs, J., 2018. Theta and alpha oscillations are traveling waves in the human neocortex. *Neuron* 98, 1269–1281.e4. doi:10.1016/j.neuron.2018.05.019.